Green Chemistry

PAPER

View Article Online
View Journal | View Issue

Cite this: *Green Chem.*, 2022, **24**, 4061

Silicon carbide (SiC) derived from agricultural waste potentially competitive with silicon anodes†

Mengjie Yu,[a] Eleni Temeche,[b] Sylvio Indris,[c] Wei Lai[d] and Richard M. Laine *[a,b]

Received 16th February 2022,
Accepted 20th April 2022

DOI: 10.1039/d2gc00645f

rsc.li/greenchem

Biomass-derived materials offer low carbon approaches to energy storage. High surface area SiC w/wo 13 wt% hard carbon (SiC/HC, SiC/O), derived from carbothermal reduction of silica depleted rice hull ash (SDRHA), can function as Li^+ battery anodes. Galvanostatic cycling of SiC/HC and SiC/O shows capacity increases eventually to >950 mA h g^{-1} ($Li_{1.2-1.4}SiC$) and >740 mA h g^{-1} ($Li_{1.1}SiC$), respectively, after 600 cycles. *Post-mortem* investigation *via* XRD and ^{29}Si MAS NMR reveals partial phase transformation from 3C- to 6H-SiC, with no significant changes in unit cell size. SEMs show cycled electrodes maintain their integrity, implying almost no volume expansion on lithiation/delithiation, contrasting with >300% volume changes in Si anodes on lithiation. Significant void space is needed to compensate for these volume changes with Si in contrast to SiC anodes suggesting nearly competitive capacities. ^6Li MAS NMR and XPS show no evidence of Li_xSi, with Li preferring all-C environments supported by computational modeling. Modeling also supports deviation from the 3C phase at high Li contents with minimal volume changes.

1. Introduction

The global momentum targeting new energy sources to tackle loss/replace traditional energy sources recognizes that such measures must be coupled strongly to environmental concerns.[1–3] One crucial approach replaces traditional fuel-based with sustainable energy sources, especially next-generation lithium-ion batteries (LIBs) relying on non-graphitic anodes, *e.g.* silicon (Si).

A further mandate is to develop sustainable batteries.[4,5] Any environmental impact evaluation must sum energy output and input *vis-à-vis* chemical composition, battery materials syntheses, energy consumed in fabrication, implementation, and recycling.[4–6] To this end, heavy metal containing active electrode materials generate significant greenhouse gas emissions during battery production and operation; a substantial component of "sustainability criteria".[7]

Clearly, recycling spent LIBs is of great importance from the viewpoint of protecting resources and the environment. However, LIB recycling efforts focus mainly on valuable metals, *e.g.*, cobalt, nickel, lithium, copper, *etc*. Research on recovery of graphite in spent LIBs is limited. Time- and energy-consuming purification processes are required to obtain battery-grade graphite from either synthetic or natural sources, including mining, beneficiation, impurity removal by HF treatment, graphitization to >2500 °C, producing considerable CO_2, NO_x, SO_x, and particulate emissions.[8–12]

Moreover, graphite's theoretical capacity is only 372 mA h g^{-1},[13,14] and susceptibility to lithium plating limiting fast-charging are major obstacles to improving the performance of current LIBs.[2,15] In principle, Si's high capacity (3579 mA h g^{-1}),[16–18] great natural abundance and low toxicity make it an undisputed superior candidate to replace graphite anodes.[13,14] Unfortunately, the significant volume changes (ΔV > 300%) during Li^+ alloying/dealloying and consequent poor capacity retention are fatal to commercial-scale use.[14,19,20] Multiple attempts to resolve these issues include fabrication of nano-scale Si-based materials in various designed structures,[20–22] as Si/C composites,[23–25] and derivatives, including SiO_x as potential substitutes.[18,26–28] Some commercial graphite anodes mixed with small amounts (4–10 wt%) of Si-containing materials have reached LIB markets.[18,27] Significant barriers to more efficient use of Si-based anodes remain.

Recently, silicon carbide's (SiC) potential as an anode material for LIBs has emerged. Si–C bilayer stacking offers a primary foundation for lithium intercalation. Kumari *et al.*[29] reported initial discharge capacities ≈ 1330 mA h g^{-1} with retained capacity ≈ 1200 mA h g^{-1} (200 cycles) using 50 nm-

[a]*Macromolecular Science and Engineering, University of Michigan, Ann Arbor, Michigan 48109, USA. E-mail: talsdad@umich.edu*
[b]*Department of Materials Science and Engineering, University of Michigan, Ann Arbor, Michigan 48109, USA*
[c]*Institute for Applied Materials-Energy Storage Systems (IAM-ESS), Karlsruhe Institute of Technology (KIT), Eggenstein-Leopoldshafen 76344, Germany*
[d]*Department of Chemical Engineering and Materials Science, Michigan State University, East Lansing, Michigan 48824, USA*
† Electronic supplementary information (ESI) available. See DOI: https://doi.org/10.1039/d2gc00645f

diameter SiC obtained by CVD of Si nanoparticles using methane. This initial report prompted further efforts to explore this traditionally electrochemically inactive material. Sun *et al.*[30] pyrolyzed resin-silica composites generating 3C-SiC nanofibers with 7.5 wt% free carbon finding a discharge capacity of 540 mA h g^{-1} (500 cycles). Zhao *et al.*[31] synthesized C/SiC nanowire (dia. 8–10 nm) composites by electrolyzing carbonized rice hulls (RHs), finding capacities > 1000 mA h g^{-1} (>400 cycles).[32]

Thus, renewable, biowaste-based anodes that offer performance superior to graphite without Si's attendant problems coupled with easy recycling offer significant motivation to realize truly green and sustainable energy sources. Ideally, closed carbon cycles could be maintained in energy storage devices where CO_2 generated from producing LIBs is returned photosynthetically to biomatter, in turn, used to manufacture batteries. In particular, rice hull ash (RHA), a byproduct of RHs combustion *for their fuel value*, consists typically of 80–90 wt% amorphous SiO_2 intimately mixed with unburned hard carbon (HC) at the nanoscale. RHA is considered an agricultural waste. Several earlier studies have explored using RHs or RHA in production of SiC, including our own, but almost always with an added carbon source and/or hazardous chemical treatments.[33–35] It is also worth noting that RHs with densities of <0.15 g per cc would mandate excessive capital equipment investment compared to RHA (>1 g per cc) if their use were to be scaled for commercial applications.

We previously described a method of directly extracting SiO_2 from RHA to produce silica depleted RHA (SDRHA) using an environmentally- and economically-friendly approach.[36] In principle, this approach valorizes RHA as a practical precursor to solar grade silicon (99.999% pure);[37] high surface area fumed and precipitated silicas for vacuum insulation panels;[38] high-performance electrodes for hybrid Li^+ supercapacitors;[39] and precursors for solid Li^+ electrolytes.[40]

In particular, SDRHA with controllable SiO_2:HC ratios allows more efficient use of the intimately mixed nano-SiO_2 and HC as natural starting materials for carbothermal reduction to high surface area SiC, Si_2N_2O, or Si_3N_4, *without need for external carbon sources*. Meanwhile, impurities commonly seen in biomass are concurrently eliminated *via* pre-purification of RHA and thereafter SDRHA using dilute acid and boiling water washes that provide starting materials with purities >99.9%.[41]

Here, we report that SDRHA derived SiC with HC (SiC/HC) and after simply oxidizing HC (SiC/O) as LIB anodes offer incremental capacity increases, reaching >950 and 740 mA h g^{-1} after 600 cycles, respectively. *Post-mortem* and computational modeling studies provide insight into the mechanisms whereby these SiC-based electrodes function with minimal volume change suggesting a possible alternative to Si.

2. Results & discussion

We recently reported a novel method of extracting SiO_2 from RHA *via* the direct distillation of the spirosiloxane $[(CH_3)_2C(O)CH_2CH(O)CH_3]_2Si$ coincidentally providing SDRHA with control of final SiO_2 : C mole ratios of 2 : 15–13 : 35. This finding enables the production of SiC *via* direct carbothermal reduction of RHA more rapidly and at lower temperatures than traditional methods as our approach takes advantage of the natural nanoscale mixing of SiO_2 and carbon in RHA without adding carbon and tedious milling processes, as described elsewhere.[41]

Greyish products are obtained by heating $SDRHA_{60}$ (60 wt% SiO_2, SSA ≈ 360 m^2 g^{-1}) at 1450 °C/8 h/Ar containing ≈13 wt% hard carbon, as shown in Fig. S1a† *via* isothermal TGA under O_2 (denoted as SiC/HC below). The XRD (Fig. S1b†) and FTIR (Fig. S1c†) both indicate the products are composed mainly of β-phase SiC, belonging to the cubic crystallographic system (3C).[42] It should be noted that the low-intensity peak at a lower angle than that of the (111) plane is ascribed to the presence of stacking faults (marked with *). Stacking faults occur frequently in growing SiC whiskers along (111) planes, perpendicular to the SiC whisker growth direction.[43]

Diffraction peaks observed at ≈36°, 42°, 60°, and 72°2θ are associated with diffraction from the (111), (200), (220), and (311) planes of 3C-SiC, respectively. Analysis using the Halder–Wagner method gives a lattice parameter of 4.3518(19), close to reference 3C-SiC parameters (4.348). The peak for the (111) lattice plane shows a stronger residual diffraction signal in comparison with the peak intensities of the reference 3C-SiC DB card (PDF 01-073-1708), suggesting a long axis in the ⟨111⟩ direction in the SiC structure. The peak intensity ratio of (200) to (111) plane is 5.25, while that for the reference pattern is 17.5. The significant difference in peak intensities is presumably due to more favored orientation along the (111) *vs.* (200) planes, resulting from competitive growth along the two directions. It is generally accepted that the surface energy of (111) planes in 3C-SiC is lower than other lattice planes, which leads to 3C-SiC whiskers growing preferentially along the ⟨111⟩ direction with lower formation energy.[44,45]

The Fig. S1d† SEM image reveals two distinct SiC morphologies: particles and whiskers, resulting from coinciding different reaction mechanisms during carbothermal reduction.[46–49] The BET specific surface area (SSA) is ≈204 m^2 g^{-1} for SiC/HC, and ≈42 m^2 g^{-1} SiC after oxidative removal at 500 °C/1 h/O_2 (denoted as SiC/O below), per Fig. S2a† N_2 adsorption/desorption isotherms. The broad pore size distribution in SiC/HC (Fig. S2b†) peaks at 17–24 nm, with no peaks seen for SiC/O (Fig. S2c†). HC typically exhibits high cross-linking inducing formation of nanopores within the disordered structures, an inescapable factor for HC-based anodes.[50]

2.1. Electrochemical performance of SiC/HC and SiC/O

SiC was long regarded as electrochemically inert to Li^+ and as a matrix to strengthen composite electrodes to mediate charge/discharge volume changes.[51–53] However, recent pioneering studies[29–31,54–58] inspired us to assess SDRHA derived SiC anodes, especially because they are synthesized readily from sustainable materials. Fig. 1a presents cross-sectional SEMs of a representative SiC/HC anode. The active materials

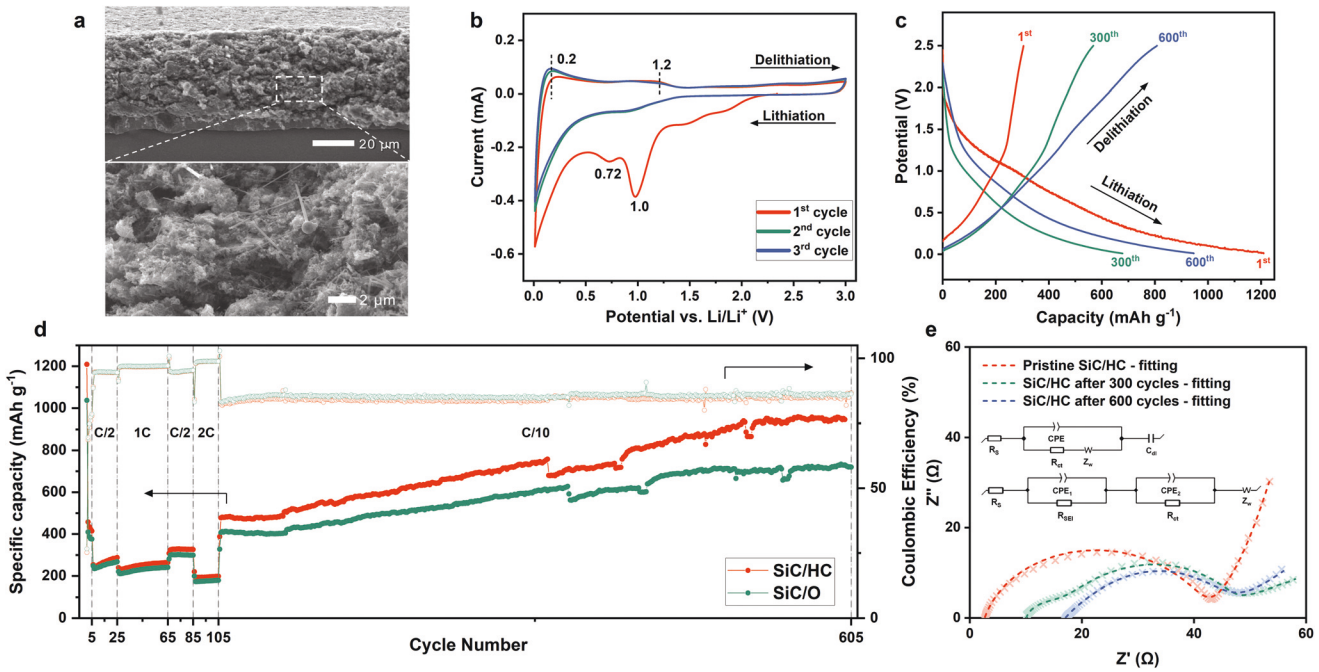

Fig. 1 (a) SEM images of cross-section of SiC/HC electrode, (b) CV scanning curves of SiC/HC, (c) charge/discharge curves of SiC/HC, (d) specific capacity *vs.* cycle number of SiC/HC and SiC/O, and (e) Nyquist plots (equivalent circuit model) of SiC/HC half cells before and after 300 and 600 cycles at 0.1C (inset: equivalent circuits).

loading is ≈1 mg cm^{-2}, giving an areal capacity of ≈0.75 mA h cm^{-2}. Both SiC/HC and SiC/O half-cell electrodes were assembled with Li metal as the counter electrode.

Fig. 1b provides CV curves for SiC/HC cycled between 3 and 0.01 V at 1 mV s^{-1}. In the first cathodic sweep, peaks appear at ≈1 and ≈0.72 V attributable to two carbonate reductive decomposition steps as the SEI forms on the anode surface. These steps disappear in subsequent scans, indicating a stable SEI.[59–61] Two oxidation peaks appearing at ≈0.2 and ≈1.2 V in anodic scans of both SiC/HC and SiC/O (Fig. S3b†) can be ascribed to Li^+ extraction. The reduction peak intensity at ≈1.2 V is lower in the 2nd and 3rd sweeps, presumably due to slow lithiation. Long plateaus appear between 0–2 V in Fig. 1c SiC/HC charge/discharge curves of Fig. S3c† for SiC/O. Fig. S3a† differential capacity analyses offer peaks at ≈0.2 and ≈1.2 V, in agreement with the CV results.

Initial SiC/HC and SiC/O half-cell discharge capacities are ≈1200 and ≈1040 mA h g^{-1}, respectively, indicating HC facilitates lithiation. However, initial Coulombic efficiencies (ICE) are both ≈25%, with subsequent reversible discharge capacities of ≈460 and ≈410 mA h g^{-1} for SiC/HC and SiC/O, respectively. The low ICEs can be ascribed to SEI formation and irreversible reactions.[62–64] The high SSAs of SiC/HC nanocomposites in the current work are likely responsible for high Li^+ consumption during initial cycles.[65]

Fig. 1d plots galvanostatic cycling capacities of SiC/HC and SiC/O half-cells. The incremental increases in capacity with cycling are a distinctive feature of SiC electrodes. On cycling at C/2 for 20 cycles and 1C for 40 cycles, SiC/HC shows discharge capacities increase from ≈250 to 270 mA h g^{-1} and ≈230 to 280 mA h g^{-1}, respectively. At 2C, capacities are ≈200 mA h g^{-1}. On cycling SiC/HC half-cells at C/10, discharge capacities reach ≈950 mA h g^{-1} (600 cycles). In comparison, HC-free SiC/O half-cells show discharge capacities ≈ 20 mA h g^{-1} lower at C/2–2C; but increases still occur. After 500 cycles at C/10, capacities reach ≈740 mA h g^{-1}.

The CEs for SiC/HC and SiC/O half-cells at C/10, C/2, 1C, and 2C are ≈85, 95, 97, and 99%, respectively. The relatively low CEs and high overpotential found for SiC/HC and SiC/O are nonideal for high-energy-density LIBs. Si-based anodes also exhibit poor later-cycle CEs from significant volume changes, particle pulverization, and repeated SEI reformation.[66] However, no previous literature discusses the origins of the typically low CEs for SiC-based anodes, as summarized in Table 1. Our studies offer some clues as to these processes, as discussed below. Optimizing CEs for SiC/HC and SiC/O anodes remains a subject for future studies.

Key comparisons with the SiC electrodes listed in Table 1 indicate SDRHA derived SiC/HC composites: (1) retain relatively higher capacities *vs.* other reported materials; (2) are readily produced by "low-temperature" (1450 °C) carbothermal reduction of an agricultural waste that is often land-filled yet can now be used perhaps at commercial levels; (3) RHA is a byproduct of RH combustion coincidentally generating 200 gigawatts and 200k tons RHA per year in the U.S. alone.[68] Given that the rice crop fixes CO_2, this process is at least carbon neutral. It may be carbon negative if land-filled RHA generates CH_4/CO_2 subsequently released to the atmosphere.

Table 1 Electrochemical performance of reported SiC anode materials

Materials	Synthesis method	Capacity[a] (mA h g^{-1})	C rate	CE[b] (%)	Initial capacity (mA h g^{-1})	ICE (%)	Capacity increments	Ref.
SiC	Commercial	443 (delithiation) after 200 c.	C/30	N/A	1537	41.1		29
SiC particle	Commercial	288 (lithiation) after 200 c.	0.1 A g^{-1}	>90*	884	48*		64
C-Coated SiC	CVD	1177 (delithiation) after 200 c.	C/30	N/A	2066	64.8		29
C-Coated SiC	Pyrolysis	350 (lithiation) after 600 c.	0.6 A g^{-1}	N/A	480	31.25	√	62
SiC nanowire	CVD	397 (delithiation) after 100 c.	C/10	94	3000	16.7*	√	56
SiC nanowire	Electro-deoxidation	720 (lithiation) after 100 c.	0.5 A g^{-1}	99.4	2266	45.5*		55
Rod-like SiC	Carbothermal reduction	400 (lithiation) after 500 c.	0.05 A g^{-1}	>90*	180	77.8*	√	31
SiC/C nanotubes	Resin/silica pyrolysis	527 (lithiation) after 250 c.	0.1 A g^{-1}	96	824	22	√	67
SiC nanofiber/C	Resin/silica pyrolysis	540 (lithiation) after 500 c.	0.3 A g^{-1}	97	309	71.7	√	30
SiC nanowire/C	Molten salt electrolysis	1120 (lithiation) after 600 c.	0.5 A g^{-1}	99	1235	65	√	31
SiC thin film	PECVD	310 (delithiation) after 60 c.	C/5	N/A	210	89	√	58
SiC thin film	ICPCVD	376 (lithiation) after 100 c.	C/3	98	1595	86		54
SiC nanoshell@hollow graphite	Sol–gel and pyrolysis	1345 (lithiation) after 600 c.	0.6 A g^{-1}	>90*	1944	36*	√	62
Epitaxial graphene@SiC	Pressure pyrolysis	968 (lithiation) after 200 c.	0.1 A g^{-1}	>90*	2051	63.4*		64
SiC/O	RHA carbothermal reduction	741 (lithiation) after 600c	C/10	85	1040	26	√	This work
SiC/HC composite		959 (lithiation) after 600c.	C/10	85	1200	25	√	

[a] Results listed in the table were tested in half-cells. Values in parentheses indicate the number of cycles (c.) to reach the capacities. [b] Values marked by * were read from figures as they were not specified in corresponding literature.

To further understand the performance of SiC/HC anodes, electrochemical impedance spectra (EIS) were run before and after cycling. In the Fig. 1e Nyquist plots, pristine SiC/HC shows one semicircle at high-to-middle frequency ranges from charge transfer resistance (R_{ct}), while the lower intercept relates to the interphase resistance (R_S), including ionic resistance of the electrolyte, the intrinsic resistance of the active materials and the contact resistance between the anode material and the current collector.[69,70] The tail in the low-frequency portion towards a vertical line where the imaginary part of impedance rapidly increases, which is a characteristic of capacitive behavior of ion diffusion due to the presence of HC in the electrode,[71,72] which exhibits a ≈45° linear Warburg resistance diffusion drift after cycling.

Corresponding equivalent circuit fitting (inset Fig. 1d) is consistent with experimental results. Accordingly, R_S for SiC/HC electrodes before and after 300 and 600 cycles are calculated as ≈3, 10, and 36 Ω, while the R_{ct} values ≈39, 30, and 24 Ω, respectively. These suggest improved charge transfer within SiC/HC composites as the electrode is activated and increased lithium contents from irreversible conversion and/or lithium plating resulting in subsequent loss of contact between active materials on cycling, which correlates with the relatively low CEs. Nevertheless, SiC/HC after 300 and 600 cycles exhibits an additional semicircle at high-frequency, corresponding to a stable R_{SEI} of ≈4.5 Ω.

The SiC/O electrode was used for galvanostatic intermittent titration technique (GITT) assessment to eliminate HC effects.[73] The Li^+ diffusion coefficients (D) run 10^{-22}–10^{-14} cm^2 s^{-1}, per Fig. S4,† which decrease at higher SOCs, maximizing at ≈14% lithiation (discharge) presumably attributable to reduced potential differences and fewer occupied sites that deactivate ion transport.[74,75]

2.2. Lithiation mechanisms

As discussed above, although incremental capacity increases were observed previously, their origins remain controversial. Reported explanations include (1) crystal structure transformation arising from Li^+ intercalation; (2) displacement reactions typical of conversion reactions resulting in slow formation of Si, C, and/or $LiSi_xC_y$; (3) slow and complex SEI formation.[64] To further investigate SiC lithiation mechanisms, *post-mortem* studies were conducted after 600 cycles.

Recovered electrodes were first cleaned (see methods section). Fig. 2a compares XRDs of SiC/HC before/after cycling. The broad hump centered ≈ 25°2θ in cycled SiC/HC is ascribed to amorphous carbon used in electrodes. In addition to peaks assigned to 3C-SiC, XRDs of cycled SiC/HC exhibit weak peaks at ≈ 38°, 41°, 44°, 55°, 64°, and 75°2θ, corresponding to (103), (104), (105), (107), (109), (204) planes of 6H-SiC, respectively. Lattice parameters for 3C-SiC increase from 4.3518(19) to 4.3533(6) Å after 600 cycles, possibly indicating slight structural changes.

SiC polytype transformation during charge/discharge was observed by Kumari *et al.*,[29] who found 8H-SiC after cycling 3C-SiC nanoparticles. They suggest this transformation is

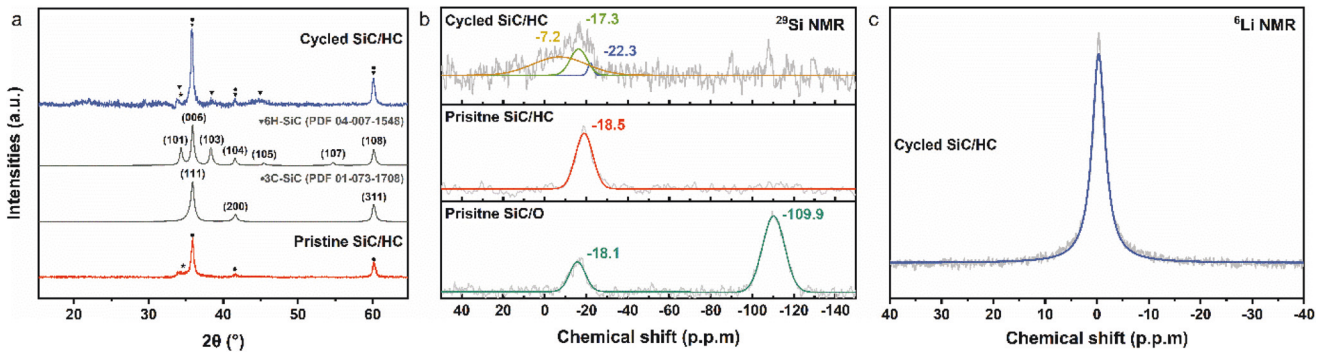

Fig. 2 (a) XRD of pristine and cycled SiC/HC, (b) ^{29}Si MAS NMR spectra of cycled SiC/HC compared with pristine SiC/HC and SiC/O, and (c) ^{6}Li MAS NMR spectra of cycled SiC/HC.

related to the incremental capacity increases. Subsequently, Li *et al.*[62] describe 3C-SiC nanoshell transformation to 6H-SiC in encapsulated, hollow graphite spheres. DFT calculations by Bijoy *et al.*[76] suggest formation of an intermediate planar structure during polytype transformation.

More definitive analytical efforts appear necessary to better resolve these unresolved issues. Thus, ^{29}Si and ^{6}Li MAS NMR studies were run to identify surface and bulk structural changes. The Fig. 2b ^{29}Si NMR of pristine SiC/HC shows a strong peak for 3C-SiC at −18.5 ppm,[77] consistent with XRD and FTIR results. An additional peak found in the SiC/O samples centered at −109.9 ppm is associated with amorphous SiO_x,[78–80] originating from oxidative removal of HC.

After cycling, the ^{29}Si signal broadens, likely from structural disorder arising during lithiation/delithiation.[81] Deconvoluting this broad peak by Gaussian fitting finds two additional peaks. 6H-SiC typically shows peaks at −20 to −22 ppm, −14 to −17 ppm, and −25 to −27 ppm in ^{29}Si spectra.[78,82] Thus, the fitted peak at −22.3 ppm is assigned to hexagonal SiC and/or intermediate phases. Insufficiently delithiated Si electrodes are reported to also show broadened ^{29}Si peaks, reflecting distributions of local environments.[83] The broad peak at −7.2 ppm suggests irreversible-lithiation of SiC and/or amorphization during lithiation/delithiation. In addition, the ^{6}Li MAS NMR of lithiated SiC/HC generates a broad peak ≈ −0.3 ppm (Fig. 2c), suggesting Li^+ is located in an amorphous phase with a strong diamagnetic environment, typical of carbon environments.[84,85] These results are common to cycled electrodes due to SEI formation. There is no evidence for formation of well-crystallized Li_xSi or Li_xC phases.

Electrode surface changes were studied using XPS, as presented in Fig. 3. Pristine SiC/HC and SiC/O show major peaks at 98, 153, 284, and 528 eV corresponding to Si 2p, Si 2s, C 1s, and O 1s, respectively. A small F 1s peak ascribed to the PVDF binder used in electrode fabrication appears at ≈690 eV. In cycled electrodes, the Si peaks are almost negligible, indicating the formation of an SEI layer. Table S1† records the quantitative analyses from XPS survey scan of SiC electrodes before and after cycling.

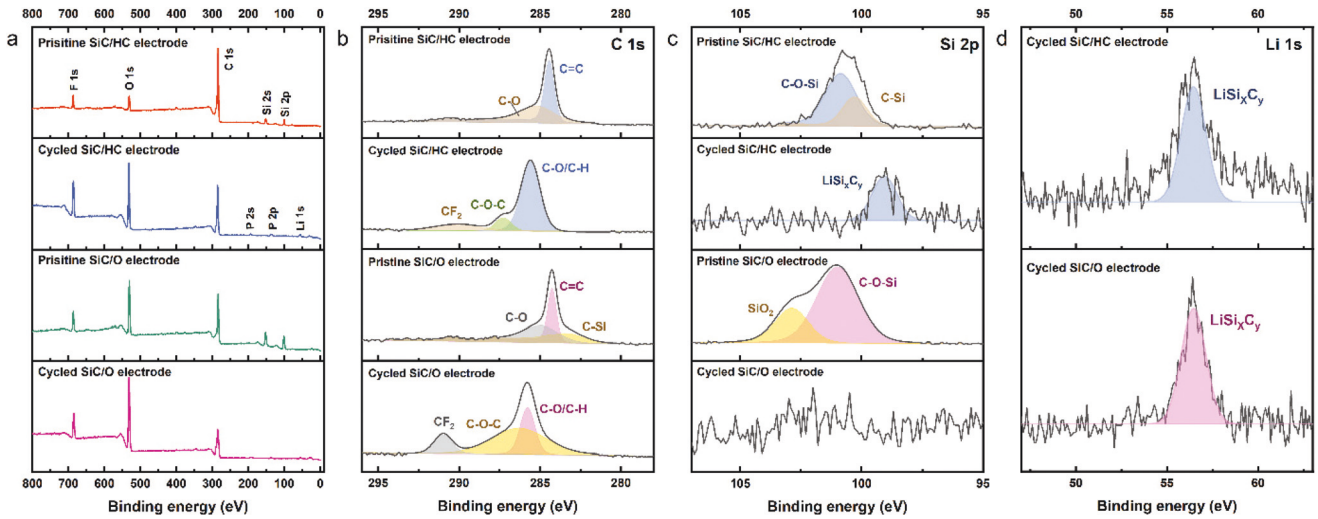

Fig. 3 (a) Wide-scan survey XPS spectra, (b) C 1s (c) Si 2p, and (d) Li 1s core level spectra of SiC/HC and SiC/O electrodes before and after 600 cycles.

The stronger F 1s peak and coincident P 2p peak in cycled electrodes can be ascribed to $LiPF_6$ electrolyte decomposition. It should be noted that the slight P 2p shift to lower binding energy (BE) from pure $LiPF_6$ (138.2 eV) is often observed for small amounts of lithium salts at electrode surfaces due to XPS differential charging effects induced by insulating species at the surfaces.[86,87]

The C 1s core spectra presented in Fig. 3b indicate both pristine SiC/HC and SiC/O electrodes show mainly deconvoluted peaks of C–Si, while C═C and C–O from the conductive additives, as summarized in Table S2.† Peaks at 290 eV (CF_2) and the wide 287–290 eV peak are visible in C 1s core spectra of both cycled SiC/HC and SiC/O electrodes, originating from the SEI surface.

Deconvolution analyses of the Si 2p core spectra in Fig. 3c reveal Si–C (100.9 eV) and C–O–Si (100.3 eV) bonds in the pristine SiC/HC electrode, while the small, broad peak at ≈99 eV in Si 2p core spectra can be attributed to irreversible amorphous $LiSi_xC_y$ species in cycled electrodes. Pristine SiC/O also shows a peak at 102.9 eV assigned to SiO_x ($x \leq 2$). No Si core level peak was observed in cycled SiC/O electrodes, presumably due to the relatively higher amounts of decomposed components on the surface, as suggested in the C 1s spectra. The Li 1s spectra of both cycled electrodes show a peak at ≈56.5 eV associated with LiF, Li_xPF_y, $Li_xPF_yO_z$, and Li-bearing organics.[88] However, no peaks appear for elemental Si, Li_xSi, or Li_xC in either spectrum, agreeing with MAS NMR observations.

Fig. 4 SEMs present microstructures of pristine and cycled SiC/HC and SiC/O electrodes, both consisting of larger (2–10 μm) particles after 600 cycles, indicating stable and robust SEI layers remain on extended cycling. Whiskers also remain, although are not dominant features. Overall, the electrodes maintain their integrity without significant volume changes on aging, suggesting the cubic to hexagonal phase transition does not alter the initial SiC electrode structure and/or morphology. EDX mapping in Fig. S5† shows uniformly distributed Si, C, O, and F in pristine electrodes and P after cycling, supporting the XPS analyses.

These results contrast greatly with Si electrodes, which suffer from pulverization and shortened cycle lives due to the high ΔV during cycling.[14,66] Highly precise measurements of volume changes are undoubtedly valuable and likely require *in operando* analyses; best done after further optimization of current materials.

Nevertheless, modeling provides additional insight into the lithiation mechanism. To model lithiation of 3C-SiC, 4, 8, and 16 Li atoms were initially placed at the tetrahedral interstitial sites of either Si (named as Si–Td) or C (C–Td), in the supercell with 32 Si and 32 C atoms. Analysis of MD trajectories suggest that Li prefers to stay at C–Td: if Li atoms were initially at placed at Si–Td, they move to C–Td; if Li atoms were initially at C–Td, they would stay there, and no diffusion could be detected within 13 ps at 1200 K. This slow Li diffusion is consistent with the experimental observation of improved capacities on long-term cycling of SiC electrodes, explaining the relatively high overpotential needed to overcome the initial activation energy barrier.

In addition, MD simulations suggest that Li_xSiC maintains the cubic phase at $x = 0.125$ and 0.25, deviating from cubic at $x = 0.5$. This phase transformation may explain the higher than theoretical capacity observed experimentally.

The SiC/O oxidized surfaces likely provide a second explanation for the differences observed and the SiC modeled here.[90–92] Easily oxidized SiC surfaces always contain Si–O species,[41] reflected in MAS NMR and XPS. In principle, SiO_x species can also contribute to capacities *via* $2x\ Li + SiO_x \rightarrow x\ Li_2O + Si$ and subsequent alloying/dealloying reactions.[89]

However, the characterization data are absent elemental Si or amorphous Li_xSi, suggesting minimal SiO_x contributions. Nevertheless, the 950 mA h g^{-1} value for SiC/HC requires

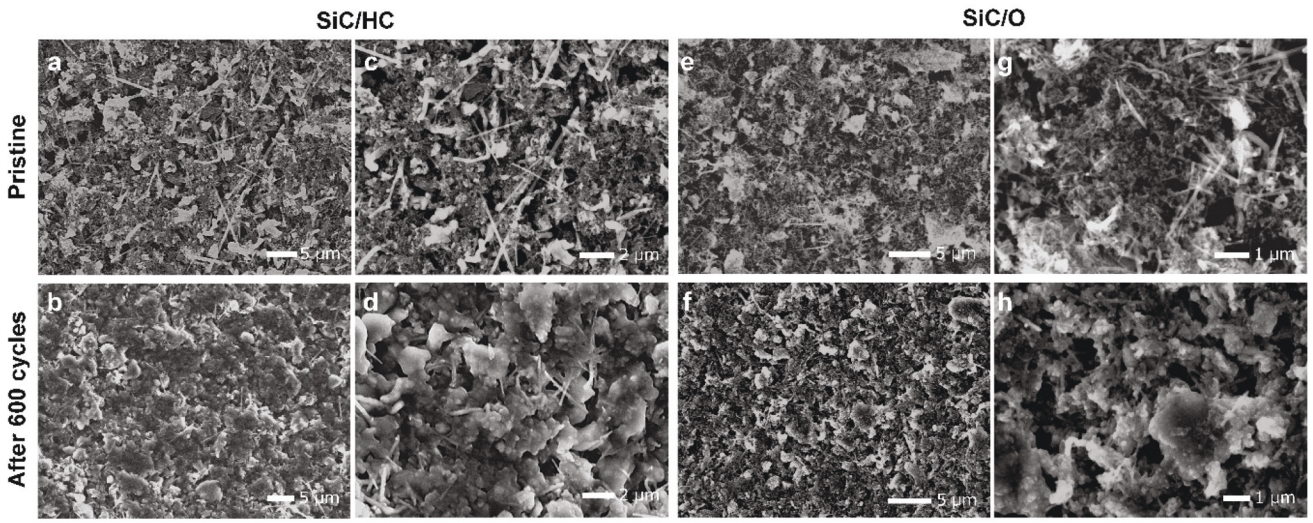

Fig. 4 SEM images of (a, c) pristine, (b, d) cycled SiC/HC electrodes, (e, f) pristine, and (g, h) cycled SiC/O electrodes.

further consideration. HC lithiation mechanisms are unclear, with capacities depending largely on the degree and type of disorder.[93] It is widely accepted that HC exhibits specific capacities of 500–700 mA h g^{-1} after heat-treating at ≈1000 °C, while heating >1000 °C promotes graphene sheet growth lowering capacities to <200 mA h g^{-1}.[94,95] Accordingly, if HC contributes to this capacity, 13 wt% HC would contribute no more than ≈ 20–90 mA h g^{-1}; thus, ≈ 160–230 mA h g^{-1} remains unaccounted for but likely arises from interfaces between 3C- and 6H-SiC, or also from stacking faults.

One reasonable conclusion is that this system lithiates to form a material with $Li_{1.2–1.4}SiC$. This has important implications about realistic SiC anode *vs.* Si-based anodes capacities; see below.

3. Conclusions

SiC/HC and SiC/O nanocomposite anodes derived from RHA are potential alternatives to graphite and competitors to Si anodes in future LIBs. SiC/HC undergoes incremental capacity increases to >950 mA h g^{-1} after 600 cycles with ambient Li^+ diffusion coefficients of 10^{-22}–10^{-14} cm^2 s^{-1} as measured by GITT.

Post-mortem characterization of cycled electrodes using XRD, ^{29}Si NMR, XPS, and SEM indicate partial phase transformation from cubic (3C) to hexagonal (6H) SiC, with no significant volume changes or surface cracking observed in SEMs. No elemental Si, Li_xSi, or Li_xC is observed, suggesting SiC lithiation is limited by intercalation rather than conversion or alloying reactions. Computational modeling suggests that a cubic to hexagonal phase transition occurs at high Li contents and indicates that Li prefers the tetrahedral C site due to electrostatic interactions.

Experimental data indicate that lithiated SiC reaches a composition of $Li_{1.2–1.4}SiC$ without significant volume changes resulting in capacities approaching ≈1000 mA h g^{-1}. Thus SiC may offer a realistic alternative to Si. The arguments in favor of this conclusion come from the fact that lithiation of Si to $Li_{4.4}Si$ occurs with ΔV > 300%, meaning that cells with Si anodes must accommodate a significant fraction of this volume change.

This allows the conclusion (disregarding mechanical property issues) that, due to the required ≈40–60% void space needed in a host material, the actual capacity of a realistic Si-based anode would be half of 3579 or 1300 mA h g^{-1} at best. A recent study reported mesoporous Si films made from wafer sawed single crystals showing specific capacities of 1200 mA h g^{-1} for 450 cycles[96] offering justification for our estimate. Additionally, SiC could eliminate surface protection needed for Si-based anodes in part as well. At this point, SiC becomes competitive.

There are clear challenges to making SiC a truly viable anode material, including fully understanding the open circuit potential, learning to optimize the overpotential and speed capacity increases such that one can reach feasible capacities in many fewer than 600 cycles, and demonstrating the realistic utility of SiC in full-cell formats.

A further point to be made is that because one can start from RHA, an agricultural waste available in 200k tons per year (U.S. alone) and which allows production of SiC/HC and SiC/O (>99.9% pure) at temperatures of 1400–1500 °C (much lower than typical carbothermal reductions) and much lower than used to produce graphite and metallurgical grade Si even from SDRHA. It may also be possible to use energy generated by RH combustion, allowing a true carbon neutral approach. Finally, SiC is an extremely hard material that could have a second life simply as an abrasive offering at least one option for facile recycling.

4. Material and methods

4.1. Synthesis of SiC from silica-depleted rice hull ash (SDRHA)

The detailed extraction of SiO_2 from RHA (Wadham Energy Inc.) to recover SDRHA and distill spirosiloxane was reported elsewhere.[36,97,98] Synthesis of SiC *via* carbothermal reduction of the SDRHA with various SiO_2 : C ratios was detailed recently.[41] In brief, (60 wt% SiO_2) powders were placed in a covered graphite crucible. On heating at 1450 °C/8 h/10 °C/min/Ar produces SiC/HC (≈85/15). The excess hard carbon can be removed by oxidizing at 500 °C/1 h/O_2.

4.2. SiC half-cell assembly

SiC/HC and SiC/O electrodes were prepared with 70 wt% SiC/HC or SiC/O, 20 wt% C_{65}, and 10 wt% poly(vinylidene fluoride) (PVDF) binder. SiC powders and C_{65} were dried at 80 °C/vacuum overnight and dry-mixed by mortar and pestle, which was then mixed with PVDF binder solution (5 wt% solution in NMP) and 1.5 g NMP in a 16 mL vial. The mixtures were ball-milled with yttria-stabilized zirconia media (3 mm dia.) overnight to obtain uniform slurries, then coated onto a copper foil (16 μm thick) using a wire-wound rod coater at a controlled speed of 50 mm s^{-1}. After drying at 80 °C/vacuum/2 h, 18 mm dia. electrodes were punched out. SiC anode porosities were calculated by: $1-(\frac{0.7\times m}{\rho_{\text{active}}}+\frac{0.1\times m}{\rho_{C_{65}}}+\frac{0.2\times m}{\rho_{\text{pvdf}}})/(S\times H)$, where m is the total mass coated on current collector, ρ_{active}, ρ_{c65} and ρ_{pvdf} are the densities of active materials (SiC, 3.21 g cm^{-3}), super C_{65} carbon black (1.6 g cm^{-3}) and PVDF (1.78 g cm^{-3}), respectively. S is the area of electrode, and H is the thickness of the coating on the current collector.

Half-cells (2023 coin cell) were assembled with SiC/HC and SiC/O electrodes, with Li metal used as the counter electrode in a glovebox. The metallic Li (16 mm × 750 μm, Alfa Aesar) was scraped to remove the oxide layer and expose a clean surface before cell assembly. Celgard 2400 (19 mm) was used as a separator and 1.1 M $LiPF_6$ in EC : DC : DMC (1 : 1 : 1weight ratio) with 10 wt% FEC additive as the electrolyte.

4.3. Material characterization

A Fourier-transform infrared spectroscopy (FTIR) Nicolet 6700 Series FTIR spectrometer (Thermo Fisher Scientific, Inc.) was used to collect FTIR spectra. X-ray diffraction (XRD, Rigaku Miniflex) was measured with Cu-Kα radiation (k = 0.154 nm) in the 2θ over the ranges of 10–80° 2θ to identify the crystallinity nature and phases. Micromeritics ASAP 2020 sorption analyzer was used for BET specific surface area (SSA) analyses. Samples were degassed at 300 °C/6 h prior to analyses by N_2 physisorption at −196 °C (77 K). BET method using 10 data multipoint with relative pressures of 0.05–1 was applied. The pore volume was calculated based on the Barret–Joyner–Halenda (BJH) model. JSM-IT300HR In Touch Scope SEM (JEOL USA, Inc.) was used to acquire the microstructure images and EDX maps. Q600 simultaneous TGA/DSC (TA Instruments, Inc.) was used for thermogravimetric analysis (TGA). Magic-angle spinning (MAS) nuclear magnetic resonance (NMR) spectroscopy ^{6}Li and ^{29}Si magic-angle spinning (MAS) nuclear magnetic resonance (NMR) spectroscopy was performed with a Bruker Avance 500 MHz spectrometer at a magnetic field of 11.7 T, corresponding to resonance frequencies of 73.6 and 99.4 MHz, respectively. Spinning was performed in 2.5 mm rotors at 30 kHz. Spectra were acquired with a π/2 pulse duration of 2.8 μs for ^{6}Li and 1.8 μs for ^{29}Si, and a recycle delay of 30 s for ^{6}Li and 60 s for ^{29}Si. X-ray photoelectron spectroscopy (XPS) was done using the Kratos Axis Ultra (Kratos Analytical) at room temperature under 3.1 × 10^{-8} Pa using monochromatic Al source (14 kV and 8 mA) to record the core level atoms. The binding energies of all the elements were calibrated relative to C 1s at 284.8 eV.

4.4. Electrochemical measurements

Data shown in the article was averaged of three cells. The galvanostatic cycling of the half-cells was performed between 0.01–2.5 V *vs.* Li/Li^+ using a multi-channel Maccor test system. The experimental mole of Li in lithiated SiC was calculated per $n_{Li} = Q_{experimental}/F \times M_{SiC}$, where F is the Faraday constant, and M_{SiC} is 40.096 g mol^{-1}.

A Bio-Logic SP-300 was used to measure the open-circuit voltage, the AC impedance, cyclic voltammetry (CV), and galvanostatic intermittent titration technique (GITT). The EIS data was recorded in a frequency range of 7 MHz to 1 Hz with an AC amplitude of 10 mV. The CV tests were conducted in the range of 0.01–3 V with a scan rate of 0.1 mV s^{-1}. The GITT tests were applied to the half-cells between 0.01–3 V at a 0.1C rate for 10 minutes, followed by resting periods of 20 min. The potential change of the current pulse *vs.* the square root of time ($\tau^{1/2}$) exhibits linear behavior with R^2 of ≈0.91 (Fig. S4b†).[99,100] The ion diffusion coefficient (D) was calculated per $D = \frac{4}{\pi\tau}\left(\frac{n_M \times V_M}{A_e}\right)^2\left(\frac{\Delta E_S}{\Delta E_\tau}\right)^2$ where n_M is the moles of active material, A_e is the contact area between the electrolyte and electrode, ΔE_s is the steady-state voltage change, and ΔE_τ is the voltage change after eliminating the IR drop during the constant current pulse.[73,99,101]

The SiC/HC and SiC/O half-cells after completing the 600 cycles test were decrimped in a dry room. The recovered electrodes were rinsed and soaked in DEC solvent to remove electrolyte salt residues that are not inherent to the SEI prior to dissolving the PDVF binder in NMP using ultrasonication. The electrodes were then dried overnight under vacuum at room temperature. The coatings on the SiC electrodes after cycling for 600 cycles were also scraped from the current collector using a razor blade in a dry room to gain better resolution active materials with eliminating the detection of Cu in following characterization.

4.5. Modeling

Density-functional theory based molecular dynamics (DFT-MD) simulations under the isobaric–isothermic ensemble were performed by the VASP package utilizing the Projector Augmented-Wave (PAW) method.[102,103] DFT calculations were performed with the PBEsol exchange–correlation functional,[104] a plane-wave cutoff energy of 550 eV, and a single k (Gamma) point. MD simulations were performed for 13 ps at an elevated temperature of 1200 K, in order to accelerate the dynamics. Atomic charges and bond orders were in the DDEC6 scheme.[105] The supercell of 3C-SiC contains 64 atoms.

Conflicts of interest

There are no conflicts to declare.

Acknowledgements

We acknowledge supports from DMR NSF Grant No. DMR-1926199 and a generous gift from Mercedes-Benz Research & Development North America (MBRDNA) for this work. We appreciate the advice provided by Dr Gregory Less at the University of Michigan Battery Lab, and the technical support from Van Vlack lab and Michigan Center for Materials Characterization. We also thank the gift of rice hull ash from Wadham Energy Inc. and Clara Huang's assistance on SDRHA synthesis.

References

1 V. Pellegrini, S. Bodoardo, D. Brandell and K. Edström, *Solid State Commun.*, 2019, **303–304**, 113733.
2 Y. Liu, Y. Zhu and Y. Cui, *Nat. Energy*, 2019, **4**, 540–550.
3 A. Tomaszewska, Z. Chu, X. Feng, S. O'Kane, X. Liu, J. Chen, C. Ji, E. Endler, R. Li, L. Liu, Y. Li, S. Zheng, S. Vetterlein, M. Gao, J. Du, M. Parkes, M. Ouyang, M. Marinescu, G. Offer and B. Wu, *eTransportation*, 2019, **1**, 100011.
4 C. Liedel, *ChemSusChem*, 2020, **13**, 2110–2141.
5 D. Larcher and J.-M. Tarascon, *Nat. Chem.*, 2015, **7**, 19–29.
6 S. Dühnen, J. Betz, M. Kolek, R. Schmuch, M. Winter and T. Placke, *Small Methods*, 2020, **4**(7), 2000039.

7 M. Romare and L. Dahllöf, *IVL Swedish Environmental Research Institute Ltd.*, 2017, 58.
8 C. Liang, Y. Chen, M. Wu, K. Wang, W. Zhang, Y. Gan, H. Huang, J. Chen, Y. Xia, J. Zhang, S. Zheng and H. Pan, *Nat. Commun.*, 2021, **12**, 119.
9 O. Fromm, A. Heckmann, U. C. Rodehorst, J. Frerichs, D. Becker, M. Winter and T. Placke, *Carbon*, 2018, **128**, 147–163.
10 J. Peng, N. Chen, R. He, Z. Wang, S. Dai and X. Jin, *Angew. Chem., Int. Ed.*, 2017, **56**, 1751–1755.
11 A. D. Jara, A. Betemariam, G. Woldetinsae and J. Y. Kim, *Int. J. Min. Sci. Technol.*, 2019, **29**, 671–689.
12 I. Rey, C. Vallejo, G. Santiago, M. Iturrondobeitia and E. Lizundia, *ACS Sustainable Chem. Eng.*, 2021, **9**, 14488–14501.
13 J. Lu, Z. Chen, F. Pan, Y. Cui and K. Amine, *Electrochem. Energy Rev.*, 2018, **1**, 35–53.
14 A. F. Gonzalez, N.-H. Yang and R.-S. Liu, *J. Phys. Chem. C*, 2017, **121**, 27775–27787.
15 Q. Liu, C. Du, B. Shen, P. Zuo, X. Cheng, Y. Ma, G. Yin and Y. Gao, *RSC Adv.*, 2016, **6**, 88683–88700.
16 H. Yang, C. Guo, A. Naveed, J. Lei, J. Yang, Y. Nuli and J. Wang, *Energy Storage Mater.*, 2018, **14**, 199–221.
17 B. Zhu, X. Wang, P. Yao, J. Li and J. Zhu, *Chem. Sci.*, 2019, **10**, 7132–7148.
18 M. Ko, S. Chae, J. Ma, N. Kim, H.-W. Lee, Y. Cui and J. Cho, *Nat. Energy*, 2016, **1**, 1–8.
19 J. R. Szczech and S. Jin, *Energy Environ. Sci.*, 2010, **4**, 56–72.
20 X. Su, Q. Wu, J. Li, X. Xiao, A. Lott, W. Lu, B. W. Sheldon and J. Wu, *Adv. Energy Mater.*, 2014, **4**, 1300882.
21 M. Ashuri, Q. He and L. L. Shaw, *Nanoscale*, 2015, **8**, 74–103.
22 K. Eom, T. Joshi, A. Bordes, I. Do and T. F. Fuller, *J. Power Sources*, 2014, **249**, 118–124.
23 Y. Lu, P. Chang, L. Wang, J. Nzabahimana and X. Hu, *Funct. Mater. Lett.*, 2019, **12**, 1850094.
24 R. Yi, F. Dai, M. L. Gordin, S. Chen and D. Wang, *Adv. Energy Mater.*, 2013, **3**, 295–300.
25 M. Xia, Y. Li, Y. Wu, H. Zhang, J. Yang, N. Zhou, Z. Zhou and X. Xiong, *Appl. Surf. Sci.*, 2019, **480**, 410–418.
26 Z. Liu, Q. Yu, Y. Zhao, R. He, M. Xu, S. Feng, S. Li, L. Zhou and L. Mai, *Chem. Soc. Rev.*, 2019, **48**, 285–309.
27 H. Wang, J. Fu, C. Wang, J. Wang, A. Yang, C. Li, Q. Sun, Y. Cui and H. Li, *Energy Environ. Sci.*, 2020, **13**, 848–858.
28 J. Yang, Y. Takeda, N. Imanishi, C. Capiglia, J. Y. Xie and O. Yamamoto, *Solid State Ionics*, 2002, **152–153**, 125–129.
29 T. S. D. Kumari, D. Jeyakumar and T. P. Kumar, *RSC Adv.*, 2013, **3**, 15028–15034.
30 X. Sun, C. Shao, F. Zhang, Y. Li, Q.-H. Wu and Y. Yang, *Front. Chem.*, 2018, **6**, 166.
31 Z. Zhao, H. Xie, J. Qu, H. Zhao, Q. Ma, P. Xing, Q. Song, D. Wang and H. Yin, *Batteries Supercaps*, 2019, **2**, 1007–1015.
32 B. Singh, *Waste and Supplementary Cementitious Materials in Concrete*, ed. R. Siddique and P. Cachim, Woodhead Publishing, 2018, pp. 417–460.
33 J. Xia, N. Zhang, S. Chong, D. Li, Y. Chen and C. Sun, *Green Chem.*, 2018, **20**, 694–700.
34 K. Sujirote and P. Leangsuwan, *J. Mater. Sci.*, 2003, **38**, 4739–4744.
35 C. Real, M. D. Alcalá and J. M. Criado, *J. Am. Ceram. Soc.*, 2004, **87**, 75–78.
36 R. M. Laine, J. C. Furgal, P. Doan, D. Pan, V. Popova and X. Zhang, *Angew. Chem.*, 2016, **128**, 1077–1081.
37 J. C. Marchal, D. J. Krug, P. McDonnell, K. Sun and R. M. Laine, *Green Chem.*, 2015, **17**, 3931–3940.
38 C. D. Li, M. U. Saeed, N. Pan, Z. F. Chen and T. Z. Xu, *Mater. Des.*, 2016, **1077**, 440–449.
39 E. Temeche, M. Yu and R. M. Laine, *Green Chem.*, 2020, **22**, 4656–4668.
40 X. Zhang, E. Temeche and R. M. Laine, *Green Chem.*, 2020, **22**, 7491–7505.
41 M. Yu, E. Temeche, S. Indris and R. M. Laine, *Green Chem.*, 2021, **23**(19), 7751–7762.
42 F. Yan, Y. D. Zheng, P. Chen, L. Sun and S. L. Gu, *Opt. Mater.*, 2003, **23**, 113–116.
43 P. Hu, S. Dong, X. Zhang, K. Gui, G. Chen and Z. Hu, *Sci. Rep.*, 2017, **7**, 3011.
44 W.-S. Seo, K. Koumoto and S. Aria, *J. Am. Ceram. Soc.*, 2004, **83**, 2584–2592.
45 R. J. Iwanowski, K. Fronc, W. Paszkowicz and M. Heinonen, *J. Alloys Compd.*, 1999, **286**, 143–147.
46 J. L. Blumenthal, M. J. Santy and E. A. Burns, *AIAA J*, 1966, **4**, 1053–1057.
47 C. Y. Chen, C. I. Lin and S. H. Chen, *Br. Ceram. Trans.*, 2000, **99**, 57–62.
48 A. W. Weimer, K. J. Nilsen, G. A. Cochran and R. P. Roach, *AIChE J.*, 1993, **39**, 493–503.
49 N. Klinger, E. L. Strauss and K. L. Komarek, *J. Am. Ceram. Soc.*, 1966, **49**, 369–375.
50 L.-F. Zhao, Z. Hu, W.-H. Lai, Y. Tao, J. Peng, Z.-C. Miao, Y.-X. Wang, S.-L. Chou, H.-K. Liu and S.-X. Dou, *Adv. Energy Mater.*, 2021, **11**, 2002704.
51 C. Wang, Y. Li, K. Ostrikov, Y. Yang and W. Zhang, *J. Alloys Compd.*, 2015, **646**, 966–972.
52 B. J. Jeon and J. K. Lee, *J. Alloys Compd.*, 2014, **590**, 254–259.
53 W. Wang, Y. Wang, L. Gu, R. Lu, H. Qian, X. Peng and J. Sha, *J. Power Sources*, 2015, **293**, 492–497.
54 X. D. Huang, F. Zhang, X. F. Gan, Q. A. Huang, J. Z. Yang, P. T. Lai and W. M. Tang, *RSC Adv.*, 2018, **8**, 5189–5196.
55 D. Sri Maha Vishnu, J. Sure, H.-K. Kim, R. V. Kumar and C. Schwandt, *Energy Storage Mater.*, 2020, **26**, 234–241.
56 Y. Hu, X. Liu, X. Zhang, N. Wan, D. Pan, X. Li, Y. Bai and W. Zhang, *Electrochim. Acta*, 2016, **190**, 33–39.
57 J. Liang, W. Wang, W. Yang, Z. Zhang, X. Zhang, Y. Jung and X. Dong, *Mater. Chem. Phys.*, 2020, **243**, 122618.
58 H. Zhang and H. Xu, *Solid State Ionics*, 2014, **263**, 23–26.
59 H. Zhang, X. Qin, J. Wu, Y.-B. He, H. Du, B. Li and F. Kang, *J. Mater. Chem. A*, 2015, **3**, 7112–7120.
60 L. Shi, C. Pang, S. Chen, M. Wang, K. Wang, Z. Tan, P. Gao, J. Ren, Y. Huang, H. Peng and Z. Liu, *Nano Lett.*, 2017, **17**, 3681–3687.

61 L. Zhao, D. Jing, Y. Shi, Q. Zhuang, Y. Cui, Z. Ju and Y. Cui, *Ionics*, 2020, **26**, 4813–4824.
62 H. Li, H. Yu, X. Zhang, G. Guo, J. Hu, A. Dong and D. Yang, *Chem. Mater.*, 2016, **28**, 1179–1186.
63 Z. Zhao, H. Xie, J. Qu, H. Zhao, Q. Ma, P. Xing, Q. Song, D. Wang and H. Yin, *Batteries Supercaps*, 2019, **2**, 1007–1015.
64 C. Sun, Y.-J. Wang, H. Gu, H. Fan, G. Yang, A. Ignaszak, X. Tang, D. Liu and J. Zhang, *Nano Energy*, 2020, **77**, 105092.
65 V. Agubra and J. Fergus, *Materials*, 2013, **6**, 1310–1325.
66 X. Zhao and V.-P. Lehto, *Nanotechnology*, 2020, **32**, 042002.
67 C. Shao, F. Zhang, H. Sun, B. Li, Y. Li and Y. Yang, *Mater. Lett.*, 2017, **205**, 245–248.
68 J. Prasara-A and S. H. Gheewala, *J. Cleaner Prod.*, 2017, **167**, 1020–1028.
69 L. A. Middlemiss, A. J. R. Rennie, R. Sayers and A. R. West, *Energy Rep.*, 2020, **6**, 232–241.
70 W. Choi, H.-C. Shin, J. M. Kim, J.-Y. Choi and W.-S. Yoon, *J. Electrochem. Sci. Technol.*, 2020, **11**, 1–13.
71 Q. Liu, Q. Shi, H. Wang, Q. Zhang and Y. Li, *RSC Adv.*, 2015, **5**, 47074–47079.
72 H. Zheng, Q. Qu, L. Zhang, G. Liu and V. S. Battaglia, *RSC Adv.*, 2012, **2**, 4904–4912.
73 K. Wang, Y. Jin, S. Sun, Y. Huang, J. Peng, J. Luo, Q. Zhang, Y. Qiu, C. Fang and J. Han, *ACS Omega*, 2017, **2**, 1687–1695.
74 J. H. Park, H. Yoon, Y. Cho and C.-Y. Yoo, *Materials*, 2021, **14**, 4683.
75 T. Sun, X. Yao, Y. Luo, M. Fang, M. Shui, J. Shu and Y. Ren, *Ionics*, 2019, **25**, 4805–4815.
76 T. K. Bijoy, J. Karthikeyan and P. Murugan, *J. Phys. Chem. C*, 2017, **121**, 15106–15113.
77 J. R. Guth and W. T. Petuskey, *J. Phys. Chem.*, 1987, **91**, 5361–5364.
78 *Pergamon Materials Series*, ed. K. J. D. MacKenzie and M. E. Smith, Pergamon, 2002, vol. 6, pp. 201–268.
79 B. Walkley and J. L. Provis, *Mater. Today Adv.*, 2019, **1**, 100007.
80 H. Lechert, *Berichte der Bunsengesellschaft für physikalische Chemie*, 1988, **92**, 1059–1059.
81 J. Sanz, *Defects and Disorder in Crystalline and Amorphous Solids*, ed. C. R. A. Catlow, Springer Netherlands, Dordrecht, 1994, pp. 157–188.
82 C. Dybowski, E. J. Gaffney, A. Sayir and M. J. Rabinowitz, *Colloids Surf., A*, 1996, **118**, 171–181.
83 K. Kitada, O. Pecher, P. C. M. M. Magusin, M. F. Groh, R. S. Weatherup and C. P. Grey, *J. Am. Chem. Soc.*, 2019, **141**, 7014–7027.
84 M. Letellier, F. Chevallier and F. Béguin, *J. Phys. Chem. Solids*, 2006, **67**, 1228–1232.
85 B. Key, R. Bhattacharyya, M. Morcrette, V. Seznéc, J.-M. Tarascon and C. P. Grey, *J. Am. Chem. Soc.*, 2009, **131**, 9239–9249.
86 R. Dedryvère, S. Leroy, H. Martinez, F. Blanchard, D. Lemordant and D. Gonbeau, *J. Phys. Chem. B*, 2006, **110**, 12986–12992.
87 S. Leroy, F. Blanchard, R. Dedryvère, H. Martinez, B. Carré, D. Lemordant and D. Gonbeau, *Surf. Interface Anal.*, 2005, **37**, 773–781.
88 *NIST X-ray Photoelectron Spectroscopy Database, NIST Standard Reference Database Number 20*, National Institute of Standards and Technology, Gaithersburg MD, 20899, 2000, DOI: **10.18434/T4T88K**.
89 M. Jiao, Y. Wang, C. Ye, C. Wang, W. Zhang and C. Liang, *J. Alloys Compd.*, 2020, **842**, 155774.
90 J. Moon, *Int. J. Energy Res.*, 2021, **45**, 7315–7325.
91 C. C. Nguyen, H. Choi and S.-W. Song, *J. Electrochem. Soc.*, 2013, **160**, A906.
92 Y. Matsuo, J. Taninaka, K. Hashiguchi, T. Sasaki, Q. Cheng, Y. Okamoto and N. Tamura, *J. Power Sources*, 2018, **396**, 134–140.
93 T. Abe, in *Encyclopedia of Electrochemical Power Sources*, ed. J. Garche, Elsevier, Amsterdam, 2009, pp. 192–197.
94 J. R. Dahn, T. Zheng, Y. Liu and J. S. Xue, *Science*, 1995, **270**, 590–593.
95 P. Kurzweil, *Electrochemical Energy Storage for Renewable Sources and Grid Balancing*, ed. P. T. Moseley and J. Garche, Elsevier, Amsterdam, 2015, pp. 269–307.
96 X. Zhao, N. Kalidas and V.-P. Lehto, *J. Power Sources*, 2022, **529**, 231269.
97 X. Zhang, E. Temeche and R. M. Laine, *Green Chem.*, 2020, **22**, 7491–7505.
98 E. Temeche, M. Yu and R. M. Laine, *Green Chem.*, 2020, **22**, 4656–4668.
99 N. Ding, J. Xu, Y. X. Yao, G. Wegner, X. Fang, C. H. Chen and I. Lieberwirth, *Solid State Ionics*, 2009, **180**, 222–225.
100 T. Schied, A. Nickol, C. Heubner, M. Schneider, A. Michaelis, M. Bobeth and G. Cuniberti, *ChemPhysChem*, 2021, **22**, 885–893.
101 Y. Zhu and C. Wang, *J. Phys. Chem. C*, 2010, **114**, 2830–2841.
102 G. Kresse and D. Joubert, *Phy. Rev. B*, 1999, **59**, 1758–1775.
103 P. E. Blochl, *Phys. Rev. B*, 1994, **50**, 17953–17979.
104 J. P. Perdew, A. Ruzsinszky, G. I. Csonka, O. A. Vydrov, G. E. Scuseria, L. A. Constantin, X. Zhou and K. Burke, *Phys. Rev. Lett.*, 2008, **100**, 136406.
105 T. A. Manz and N. G. Limas, *RSC Adv.*, 2016, **6**, 47771–47801.